An *ab initio* quasi-classical direct dynamics investigation of the F + C₂H₄ → C₂H₃F + H product energy distributions

An *ab initio* quasi-classical direct dynamics investigation of the
$F + C_2H_4 \rightarrow C_2H_3F + H$ product energy distributions

Kim Bolton,[†][a] H. Bernhard Schlegel,[a] William L. Hase*[a] and Kihyung Song[b]

[a] *Department of Chemistry, Wayne State University, Detroit, MI 48202, USA*
[b] *Department of Chemistry, Korea National University of Education, Chongwon, Chungbuk 363-791, Korea*

A direct dynamics technique, using energies, forces and second derivatives calculated at the UHF/6–31G* level of theory, was used to investigate product energy distributions of the $F + C_2H_4 \rightarrow C_2H_3F + H$ collision reaction. The shifting and broadening of the product translational energy distribution as the system moves from the exit-channel barrier to the products was studied. Since properties associated with the rupturing C···H bond are similar for the $C_2H_5^‡$ and $C_2H_4F^‡$ exit-channel barriers, and integration of the $C_2H_5^‡ \rightarrow C_2H_4 + H$ reaction is approximately 2.5 times faster than the $C_2H_4F^‡ \rightarrow C_2H_3F + H$ reaction, trajectories of the former reaction were propagated to gain insight into the exit-channel dynamics. Ensemble averaged results for $C_2H_5^‡$ dissociation are well described by a model based on isotropic exit-channel dynamics which assumes that the product relative translational distribution arises from the centrifugal potential and relative translational energy distributions at the exit-channel barrier plus the exit-channel potential release. The width of the product translational energy distribution is sensitive to overall rotational angular momentum and its partitioning between $C_2H_4\cdots H^‡$ orbital angular momentum and $C_2H_4^‡$ rotational angular momentum. The simulated product translational energy distribution for the $C_2H_4F^‡ \rightarrow C_2H_3F + H$ reaction is broadened by relative translation–vibrational couplings in the exit-channel and is similar to the distribution used to fit crossed molecular beam data. Approximately 50% of the available energy is in product relative translation, which also agrees with experiment. RRKM calculations indicate that a second reaction mechanism, involving 1–2 hydrogen migration prior to C···H bond fission, does not significantly contribute to $C_2H_3F + H$ product formation.

1 Introduction

A considerable amount of experimental[1–22] and theoretical[23–43] work has been done on reactions of ethene with atoms such as hydrogen, fluorine and chlorine, both because they are some of the simplest atom–olefin reactions and because there are indications that some of these reactions exhibit non-statistical effects. An example is the $F + C_2H_4 \rightarrow C_2H_3F + H$ reaction, which has been studied over a range of collision energies ($2 \leqslant E_{rel} \leqslant 12$ kcal mol⁻¹) using crossed molecular beam techniques.[4,10] In these experiments, Lee and co-workers[4,10] obtained C_2H_3F product angular and velocity distributions that are not easily interpreted using simple statistical models which neglect coupling in the exit-channel. Also, average product relative translational energies, $\langle E'_{rel} \rangle$, are *ca.* 50% of the available energy at all collision energies investigated.[4,10] It was suggested that these effects indicate non-statistical dynamics of the $C_2H_4F^*$ collision complex or strong coupling in the exit-channel. This is consistent with the infrared chemiluminescence observations of Moehlmann *et al.*[8] where a non-statistical distribution of C_2H_3F internal energy following H emission was observed.

It was noted that the product C_2H_3F internal energy distributions do not necessarily reflect the distribution at the exit-channel transition state.[8,10] Moreover, the angular distribution of C_2H_3F in the molecular beam experiments has

forward–backward symmetry,[4,10] indicating that the collision complex has a lifetime of at least one rotational period, and the fraction of product energy in vibration increased as the molecular size of the complex increased.[4] Since these observations were interpreted as showing substantial equilibration of the C_2H_4F complex energy, definitive conclusions regarding the broadening of the translational energy distribution could not be drawn.

A number of models have been advanced to reconcile theory and experiment. They differ from models that assume no coupling in the exit channel, such as phase space theory.[44,45] In Marcus's tight transition state model,[23,24] bending quanta in the transitional modes at the product barrier go to rotational quanta of the product fragments. Since the bending vibrational levels are more widely spaced than the product rotational levels, there is an excess of energy that is assumed to go to product relative translation. In another tight transition state model, developed by Safron *et al.*,[46] it is assumed that the relative translational energy of the products equals the sum of the exit-channel barrier height, E_0, and the relative translational energy and centrifugal potential at the barrier. Zvijac *et al.*[26] developed a model where the reactant, complex and product normal modes were separated into weak modes—which are weakly coupled to the relative reactant or product translation—and strong modes. By defining Frank–Condon factors between the strong modes, treating the weak modes statistically and varying the extent of energy randomization in the complex prior to C···H bond fission, they calculated product vibrational and translational energy

† Present address: Department of Chemistry, Physical Chemistry, Göteborg University, S-412 96 Göteborg, Sweden.

distributions. Kato and Morokuma[34] considered both adiabatic and sudden models for the exit-channel dynamics. By determining the amount of energy in the exit-channel barrier that is due to product deformation and the product vibrational modes that gain this energy, they were able to predict product vibrational energy distributions. Also, by projecting the transition state normal mode eigenvectors on to the product vibrational, rotational and translational modes, they could determine which modes were coupled during the exit-channel dynamics. Two vibrational modes at the transition state coupled with product relative translation, enabling energy to flow between these modes and relative product translation and leading to broadening in the E'_{rel} distribution. Although all the above models provide insight into the dynamics that affect the product energy distributions, none of them give quantitative interpretations of the experimental results.

A previous classical trajectory study, based on an analytic surface (PES),[37] showed that a stable $C_2H_4F^*$ collision complex is formed before dissociating to $C_2H_3F + H$ products. Comparison of $\langle E'_{rel} \rangle$ with the average centrifugal potential, $\langle V_{cen}^{\ddagger} \rangle$, and relative translational energy, $\langle E_{rel}^{\ddagger} \rangle$, at the exit-channel barrier, showed that about 80% of the

$$C_2H_4F^{\ddagger} \rightarrow C_2H_3F + H \qquad (R1)$$
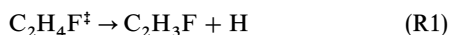
potential energy of the barrier went to translation. $\langle E'_{rel} \rangle$ was ca. 30% of the available energy, which is less than that required to fit the crossed molecular beam data (ca. 50%). Also, although the E'_{rel} distribution was broad, it was not as broad as the experimental distributions. (For the sake of brevity, the E'_{rel} distributions and averages used to fit the experimental angular and velocity distributions will be referred to as experimental distributions and averages, even though they are not directly measured in the crossed molecular beam experiments.)

Subsequent ab initio calculations[40,41] showed that the structures at the entrance and exit-channel barriers are significantly tighter than those of the analytic surface used in the trajectory study. This is seen by the higher ab initio frequencies of the transitional C···H bending modes, indicating that they are better approximated as 'reactant' vibrations than product rotations. The energy in these modes at the transition state may go to product translation, rotation and vibration,[23,34] hence the frequencies and eigenvectors of these transitional modes may influence the E'_{rel} distribution. Also, as will be discussed in Section 4, the ab initio reaction coordinate at the transition structure is not a pure C···H bond rupture. An increase in the coupling between the rupturing C···H bond and the vibrational modes may persist during the bond rupture, hence affecting the E'_{rel} distribution. Changes in the width of the entrance channel may affect the range of collision impact parameters leading to $F + C_2H_4$ association and, thus, the C_2H_4F rotational angular momentum distribution. Since the magnitude and distribution of the C_2H_4F angular momentum directly affect the magnitude and distribution of the centrifugal potential at the exit-channel barrier (which, in an isotropic exit-channel model, goes to product translation),[37] the width of the entrance channel may be an important factor in obtaining the correct E'_{rel} distribution.

In this study, the direct dynamics method was used to investigate the sensitivity of the product energy distributions, especially the E'_{rel} distribution, to the energy distribution at the $C_2H_4F^{\ddagger}$ exit-channel barrier and coupling in the $C_2H_4F^{\ddagger} \rightarrow C_2H_3F + H$ exit-channel region. Classical trajectories were integrated 'on the fly', using forces and Hessians (when required) obtained directly from ab initio electronic structure theory at each integration step. This obviated the need to construct an analytic surface so that trajectories were propagated using the 'unadulterated' forces and Hessians calculated at the chosen level of electronic structure theory.

Direct dynamics simulations based on semiempirical surfaces have met with varying degrees of success,[47–50] while an ab initio direct dynamics study of formaldehyde dissociation gave energy partitioning in agreement with experiment.[51] Other applications and results of direct dynamics methods are reviewed elsewhere.[52] This study provides a further test of the ab initio direct dynamics technique. It should be noted that the schemes proposed by Collins and co-workers[53] and Rabitz and co-workers[54] for constructing multi-dimensional molecular potential energy surfaces from ab initio calculations will give results equivalent to direct dynamics if the representation of the ab initio calculations by the surfaces is adequately converged.

Schlegel and co-workers[40,41] have shown that the stationary point geometries and frequencies for

$$C_2H_5^{\ddagger} \rightarrow C_2H_4 + H \qquad (R2)$$

have properties similar to those for reaction (R1). Since integration of reaction (R2) is ca. 2.5 times faster than integration of reaction (R1) and most properties relevant to reaction (R1) are expected to be exhibited by reaction (R2) (see Section 4), the bulk of this study is based on reaction (R2). The effect of the fluorine mass, and properties peculiar to the reaction (R1) exit-channel, are considered once the factors governing the E'_{rel} distribution for reaction (R2) have been ascertained.

Owing to the expense of ab initio calculations, this investigation was limited to ensembles of fairly short time trajectories initiated at the exit-channel barrier for reactions (R1) and (R2). Performing ab initio direct dynamics for the complete reaction, e.g., $F + C_2H_4 \rightarrow C_2H_4F \rightarrow C_2H_3F + H$, including the intramolecular motion of the C_2H_4F intermediate, is not feasible at this time. Initiating the trajectories at the exit-channel barrier, using the quasi-classical method,[55] ensures that the system has the proper zero point energy distribution at this region of the potential energy surface.[38,56] The ab initio trajectories are integrated using forces and second derivatives obtained from the UHF/6–31G* moderate level of ab initio theory, which gives accurate stationary point geometries, energies and frequencies for reaction (R1).[40,41]

This direct dynamics investigation assumes only one significant pathway for the $F + C_2H_4 \rightarrow H_2FC - CH_2 \rightarrow C_2H_3F + H$ reaction, i.e., an H atom attached to the H_2FC moiety dissociates. Another energetically reasonable pathway involves 1–2 migration of an H atom, before dissociation from the CH_3 moiety. The presence of two reaction channels could lead to a broadening in the E'_{rel} distribution, e.g., if they have different barriers for the back reaction. In the next section the importance of the migration pathway is investigated using RRKM theory.

In Section 3 the exothermicity of the $F + C_2H_4 \rightarrow C_2H_3F + H$ reaction is evaluated. The exothermicity is required to relate the energy of the trajectories, initialized at the exit-channel barrier, to the $F + C_2H_4$ relative translational energies studied in the molecular beam experiments. In Section 4, the UHF/6–31G* stationary point geometries, energies and frequencies relevant to reactions (R1) and (R2) are presented, with emphasis on the features that are relevant to the dissociation dynamics. The initialization, propagation and analysis of the classical trajectories are described in Section 5, together with the methods used to study the energetics and coupling along the exit-channel intrinsic reaction coordinate (IRC). The results are analyzed and compared with the crossed molecular beam data in Section 6, and the conclusions are presented in Section 7. A preliminary report of this study has been published.[57]

2 Branching ratios for H···FHCCH$_2$ dissociation and 1–2 migration pathways

If the potential energy of the exit-channel barrier goes to

Table 1 Minimum energy differences ($E_{0,m} - E_{0,d}$) between the $C_1 \rightarrow C_2$ migration and $C_1 \cdots H$ bond rupture barriers

Level of theory	$E_{0,m} - E_{0,d}$/kcal mol^{-1}
UHF/6–31G*	14.88(17.37)[a]
UHF/6–311G**	12.01
PMP2/6–311G**	5.25
PMP3/6–311G**	4.19
PMP4SDQ/6–311G**	4.93
QCISD/6–311G**	4.02(6.11)[a]

[a] Zero point corrected energy.

product relative translation, the presence of two competing reaction pathways with different barrier heights will lead to product fragments with different relative translational energies, and this would be seen as a broadening in the E'_{rel} distribution. In particular, in addition to $C \cdots H$ bond rupture occurring from the H_2FC moiety (*i.e.*, denoted $C_1 \cdots H$ bond rupture), it is possible that $C_1 \rightarrow C_2$ H-atom migration also occurs followed by $C_2 \cdots H$ bond rupture from the CH_3 moiety.

Energies were obtained for the stationary structures relevant to both reaction channels (*i.e.*, the $C_1 \cdots H$ and $C_2 \cdots H$ bond ruptures) at the UHF/6–31G* and QCISD/6–311G** levels of theory. (Comparison is made with UHF/6–31G* since the direct dynamics simulation is done at this level.) The UHF/6–31G* $C_1 \cdots H$ exit-channel barrier height is 6.2 kcal mol^{-1} and increases to 6.4 kcal mol^{-1} after zero point energy correction, and at the QCISD/6–311G** level it is 6.0 kcal mol^{-1} and increases to 7.1 kcal mol^{-1} after zero point energy correction. The scaling factors for the UHF/6–31G* and QCISD/6–311G** zero point energies are 0.9135 and 0.9897, respectively.[58] The exit-channel barrier height for the $C_2 \cdots H$ bond rupture is 4.0 and 3.8 kcal mol^{-1} at the UHF/6–31G* and QCISD/6–311G** levels of theory, respectively. These increase to 4.2 and 4.8 kcal mol^{-1}, respectively, on correcting for zero point energy. These are similar and are substantially lower than the exit-channel barrier for $C_1 \cdots H$ dissociation.

The importance of the $C_2 \cdots H$ bond rupture pathway depends, *inter alia*, on the relative energies for $C_1 \rightarrow C_2$ migration and $C_1 \cdots H$ bond dissociation. Table 1 lists the energy difference ($E_{0,m} - E_{0,d}$) between the $C_1 \rightarrow C_2$ migration and $C_1 \cdots H$ dissociation barriers calculated at the UHF/6–31G* level of theory and at the UHF, PMP2, PMP3, PMP4SDQ

and QCISD levels using a 6–311G** basis set. The zero point corrected energy differences are given in parentheses for the UHF/6–31G* and QCISD/6–311G** levels of theory. Although the QCISD/6–311G** zero point energy contributions for both the migration and dissociation transition structures are larger than the UHF/6–31G* contributions, the *differences* in zero point energies between these structures are similar at the two levels of theory (2.5 kcal mol^{-1} for UHF/6–31G* and 2.1 kcal mol^{-1} for QCISD/6–311G**), indicating that feasible comparisons can be made between the energy differences, before zero point energy correction, at all levels of theory.

An increase in the size of the basis set lowers the energy difference by 2.9 kcal mol^{-1} at the UHF level of theory. This is not as large as the decrease on introducing electron correlation. At the MP2 level the energy difference is reduced by *ca.* 6.8 kcal mol^{-1}. Employing higher levels of theory, *i.e.*, MP3, MP4SDQ and QCISD, does not significantly change the energy difference, indicating that the results have begun to converge. The QCISD/6–311G** energy difference (6.11 kcal mol^{-1}) is less than the UHF/6–31G* result (17.4 kcal mol^{-1}) by more than 10 kcal mol^{-1}.

RRKM branching ratios (BR) for the $C_1 \cdots H$ bond rupture and $C_1 \rightarrow C_2$ migration pathways were determined from

$$ BR = \frac{N_d^{\ddagger}(E,J)}{N_m^{\ddagger}(E,J)} \qquad (1) $$

where $N^{\ddagger}(E,J)$ is the number of rovibrational states at the transition state[59] with energy $\leqslant E$ and total angular momentum J.[60,61] To calculate $N^{\ddagger}(E,J)$, the rotational degree of freedom associated with the K quantum number is assumed to be active and a summation is made over all possible values of K.[62] The Beyer–Swinehardt algorithm[60] was employed to count the quasi-classical, harmonic vibrational states, using scaled frequencies obtained at the UHF/6–31G* and QCISD/6–311G** levels of theory (see Table 2). The scaling factor[58] used for the UHF/6–31G* frequencies was 0.8953 and for QCISD/6–311G** it was 0.9641.

Branching ratios were determined over the range of energies relevant to the crossed molecular beam experiments, *i.e.*, $2 \leqslant E_{rel} \leqslant 12$ kcal mol^{-1}. The energy E, used in eqn. (1), is

$$ E = E_{rel} - \Delta H_0^0 + D_0 \qquad (2) $$

where $\Delta H_0^0 = -12.77$ kcal mol^{-1} is the $F + C_2H_4 \rightarrow C_2H_3F$

Table 2 Scaled normal mode frequencies and moments of inertia used in the RRKM branching ratio calculations

UHF/6–31G*		QCISD/6–311G**	
$C_1 \rightarrow C_2$[a]	$C_1 \cdots H$[b]	$C_1 \rightarrow C_2$[a]	$C_1 \cdots H$[b]
Scaled frequencies[c]/cm^{-1}			
313	408	317	402
424	431	432	433
727	477	694	480
780	611	772	674
927	759	919	806
1107	901	1110	913
1149	918	1162	968
1239	1133	1258	1146
1345	1219	1347	1271
1407	1382	1402	1379
1947	1494	2116	1572
2981	3006	3053	3070
3021	3064	3088	3118
3090	3097	3178	3182
Moments of inertia/Å^2—			
10.28, 52.01, 59.06	12.42, 50.24, 56.66	10.39, 53.23, 60.33	12.23, 50.86, 57.13

[a] Migration transition structure. [b] Bond rupture transition structure. [c] Scaling factor for UHF/6–31G* frequencies is 0.8953 and for the QCISD/6–311G** frequencies it is 0.9641.[58]

+ H heat of reaction (discussed in the next section) and D_0 is the $C_2H_4F \rightarrow C_2H_3F + H$ dissociation energy, *i.e.*, it is the energy difference between the zero point levels of the products and the C_2H_4F equilibrium structure. The C_2H_4F *gauche* structure, which is 0.2 kcal mol^{-1} lower than the *anti* structure at the UHF/6–31G* level of theory,[41] was used in the calculations. UHF/6–31G* and QCISD/6–311G** energies and frequencies were evaluated for the products but, owing to the expense of the QCISD/6–311G** frequency calculations, the scaled UHF/6–31G* zero point energy of the C_2H_4F equilibrium structure was used in both the UHF/6–31G* and QCISD/6–311G** calculations, although minimum potential energies were determined at both levels of theory. D_0 at the UHF/6–31G* level is 34.2 kcal mol^{-1} and at the QCISD/6–311G** level it is 32.6 kcal mol^{-1}.

For each energy, total angular momenta of $0 \leqslant J \leqslant 90\hbar$ were considered (simulation of the $F + C_2H_4 \rightarrow C_2H_3F + H$ reaction on an analytic PES[37] showed that J ranged from 0 to $90\hbar$ for $E_{rel} \leqslant 12$ kcal mol^{-1}). The moments of inertia, required to calculate the rotational contribution to $N^\ddagger(E,J)$, are given in Table 2. Under all conditions the branching ratio was large, indicating that $C_1 \cdots H$ bond rupture dominates over $C_1 \rightarrow C_2$ migration. Using the scaled UHF/6–31G* energies and frequencies, the smallest branching ratio was 51×10^3 for $E_{rel} = 12$ kcal mol^{-1}, $J = 0$. For the QCISD/6–311G** energies and frequencies, the smallest branching ratio was 23 and also for $E_{rel} = 12$ kcal mol^{-1}, $J = 0$. Hence, based on the scaled energies and frequencies obtained at the UHF/6–316G* and QCISD/6–311G** levels of theory, the $C_1 \cdots H$ bond rupture reaction pathway (studied in this direct dynamics simulation) dominates over the $C_1 \rightarrow C_2$ migration pathway.

3 Heat of reaction

The heat of reaction, ΔH_0^0, for the $F + C_2H_4 \rightarrow C_2H_3F + H$ reaction is needed to fit the crossed molecular beam data, and is required to compare the trajectory results with the experimental data. Lee and co-workers[4,10] assumed that the E'_{rel} distribution could be described by

$$P(E'_{rel}) = N(E'_{rel} - V_a)^\alpha (E' - E'_{rel})^s \qquad (3)$$

where N is a normalization constant, V_a, α and s are fitting parameters and E' is the energy available to the products, which is the energy of the $F + C_2H_4$ reactants plus the energy released in forming the products. Since C_2H_4 was rovibrationally cold in the molecular beam experiments, the reactant energy is the energy in relative translation, E_{rel}, and

$$E' = E_{rel} - \Delta H_0^0 \qquad (4)$$

where ΔH_0^0 is the 0 K heat of reaction. Parson and Lee[4] assumed that $\Delta H_0^0 = -11$ kcal mol^{-1} and, since $E_{rel} = 2$ kcal mol^{-1} in their experiments, the distribution in eqn. (3) extended from 0 to 13 kcal mol^{-1}. In subsequent crossed molecular beam experiments,[10] ΔH_0^0 of -14 kcal mol^{-1} was assumed. Based on experimental and theoretical data, Schlegel *et al.*[4] estimated $\Delta H_0^0 = -15 \pm 2$ kcal mol^{-1}.

In this study, the trajectories are initialized at the product barrier with an energy, $E^\ddagger$, in excess of the barrier's zero point level. $E^\ddagger$ is related to E_{rel} *via*

$$E_{rel} - \Delta H_0^0 = E^\ddagger + E_0 \qquad (5)$$

E_0 is the exit-channel barrier height including zero point energy and is calculated at the level of theory used in the direct dynamics study. Once E_0 has been determined $E^\ddagger$ can be selected for a desired E_{rel} if ΔH_0^0 is known.

ΔH_0^0 was calculated from the 298 K experimental heats of formation and the 298 K enthalpies of reactants and products. At 298 K, $\Delta H_f^{C_2H_3F} = -33.17$ kcal mol^{-1}, $\Delta H_f^H = 52.10$ kcal mol^{-1}, $\Delta H_f^F = 18.98$ kcal mol^{-1} and $\Delta H_f^{C_2H_4} = 12.52$ kcal

mol^{-1},[63] hence the heat of reaction at 298 K is $\Delta H_{298}^0 = -12.57$ kcal mol^{-1}. The translational and rotational contributions to the enthalpies for the products and reactants are the same, so that only the vibrational degrees of freedom of the reactants and products contribute in determining ΔH_0^0 from ΔH_{298}^0.

Experimental frequencies were used for C_2H_4[64] and C_2H_3F[65] to calculate their 298 K vibrational enthalpies.[66] They are 826, 943, 949, 1073, 1220, 1342, 1444, 1630, 3021, 3026, 3103 and 3105 cm^{-1} for C_2H_4 and 490, 713, 863, 923, 929, 1157, 1305, 1380, 1656, 3052, 3080 and 3116 cm^{-1} for C_2H_3F. The resulting value for ΔH_0^0 is -12.77 kcal mol^{-1}, only 0.20 kcal mol^{-1} lower than ΔH_{298}^0.

4 UHF/6–31G* potential energy surface

The C_2H_3F and C_2H_4 minimum energy geometries obtained at the UHF/6–31G* level of theory[40] are shown in Fig. 1. Both of these structures are planar and are in good agreement with experiment[1,5] (values shown in parentheses). These geometries are very similar to those obtained at higher levels of theory using larger basis sets.[40] For example, optimization of the C_2H_4 structure[67] at the UHF/3–21G, UHF/6–31G*, MP2/3–21G, MP2/6–31G*, QCISD/6–311G** and MRCI/CC-pVDZ levels of theory gave bond lengths that agree with the values in Fig. 1 to within ± 0.03 Å and angles that agree within $\pm 0.5°$. Similar results were obtained for the fluorinated structure.[40] The transition structures shown in Fig. 2 are also in agreement with higher levels of *ab initio* theory.[67] Comparison of Figs. 1 and 2 shows that the C_2H_3F and C_2H_4 geometries at the transition state differ from their product geometries, especially in the out-of-plane wags and dihedrals and CC bond length. The transition state is substantially 'tighter' than the transition state obtained from the analytic PES used in the previous classical trajectory study (see Table II in ref. 37).

The exit-channel barrier heights are not converged.[41,67] The UHF/6–31G* barriers are 6.19 kcal mol^{-1} for reaction (R1) and 2.91 kcal mol^{-1} for reaction (R2). Making the small zero point energy correction, at the harmonic level, yields E_0 values of 6.39 and 3.11 kcal mol^{-1} for the two reactions. These values, which are used in the trajectory calculations, are very similar to those with scaled zero point energies, *i.e.*, 6.37 and 3.09 kcal mol^{-1}, for a scaling factor of 0.9135.[58] Using *ab*
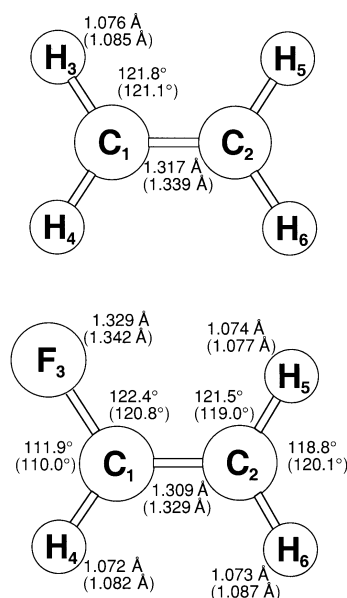
Fig. 1 C_2H_3F and C_2H_4 minimum energy geometries obtained at the UHF/6–31G* level of theory.[40] Both structures are planar. Experimental values[1,5] are shown in parentheses.
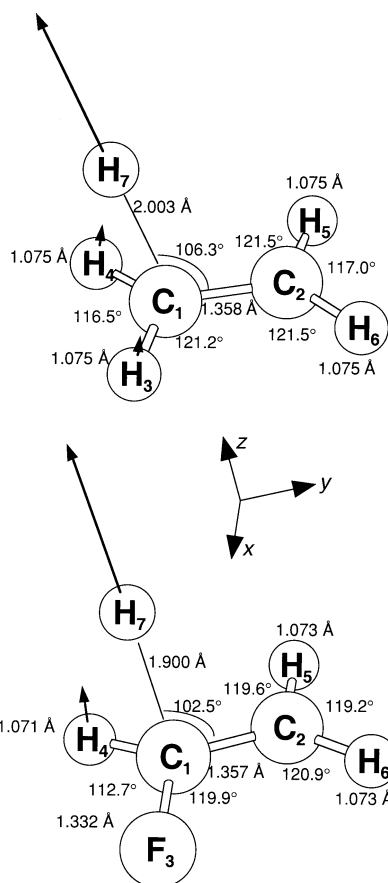
Fig. 2 $C_2H_4F^{\ddagger}$ and $C_2H_5^{\ddagger}$ transition structures obtained at the UHF/6–31G* level of theory.[40] The out-of-plane wag angles are $C_2C_1F_3H_4 = 164.8°$ and $C_1C_2H_5H_6 = 175.6°$ for $C_2H_4F^{\ddagger}$ and $C_2C_1H_3H_4 = 169.7°$ and $C_1C_2H_5H_6 = 177.4°$ for the $C_2H_5^{\ddagger}$. The reaction coordinate eigenvectors are superimposed on these structures.

Table 3 Harmonic normal mode frequencies (cm^{-1}) for the $C_2H_4F^{\ddagger}$ and $C_2H_5^{\ddagger}$ transition structures

UHF/6–31G*		Analytic PES[a]
$C_2H_5^{\ddagger}$	$C_2H_4F^{\ddagger}$	$C_2H_4F^{\ddagger}$
658i[b]	900i[b]	758i
414	456	253
446	480	290
881	533	383
930	682	398
1026	848	743
1038	1006	858
1321	1025	965
1340	1265	1098
1600	1361	1234
1693	1544	1436
3327	1669	1635
3339	3357	2934
3407	3422	2985
3431	3459	3033

[a] PES used in previous classical trajectory studies.[37] [b] Frequencies of the reaction coordinate eigenvectors illustrated in Fig. 2.

to estimate a value of 5–6 kcal mol^{-1} for this E_0,[41] in agreement with the UHF/6–31G* value.

The UHF/6–31G* harmonic normal mode frequencies for the transition structures are given in Table 3. Although calculations at various levels of *ab initio* theory yield different frequencies, they all give transition structures which are tight with respect to the bending and stretching motion of the rupturing H$\cdots$C bond. This is seen by the relatively large frequencies of the reaction coordinate and the two transitional modes associated with the H$\cdots$C bends (the imaginary frequency and two lowest orthogonal mode frequencies in Table 3). The normal mode frequencies obtained from the analytic PES are listed in the third column of the table. The reaction coordinate and transitional mode frequencies are substantially lower than those obtained at the UHF/6–31G* level of theory.

The reaction coordinate eigenvectors (obtained at the UHF/6–31G* level of theory), shown in Fig. 2, exhibit distinct HC$\cdots$H angle bending character, indicating that the reactions are not pure H$\cdots$C bond ruptures. The reaction coordinate also contains a CC stretch contribution, but since the magnitude of this contribution to the mass-weighted normal mode eigenvector is smaller than the H$\cdots$C stretching and bending contributions, it does not appear in the figure. The dot products of these eigenvectors with the unit vector describing pure C$\cdots$H bond rupture are 0.94 and 0.96 for $C_2H_4F^{\ddagger}$ and $C_2H_5^{\ddagger}$, respectively (a value of 1.0 would indicate pure bond rupture). The deviation from unity is due to HC$\cdots$H bending and CC stretching motion. The insensitivity of the (R1) reaction coordinate eigenvector to an increase in the level of theory is seen by the fact that the dot product of the reaction coordinate obtained at the UHF/6–31G* level with that obtained at the QCISD/6–311G** level is 0.99.

Fig. 2 shows that the transition structure geometries and reaction coordinate eigenvectors are similar for reactions (R1) and (R2). As seen in Fig. 1, their product geometries are also similar. Hence some of the effects of coupling between the reaction coordinate and vibrational modes that are found for reaction (R1) are also likely to be evident in the dynamics of reaction (R2).

initio structures and vibrational frequencies to fit the H + $C_2H_4 \rightarrow C_2H_5$ experimental rate constant, $E_0 = 2.70$ kcal mol^{-1} has been deduced for reaction (R2),[67] in good agreement with the UHF/6–31G* value. Since the H + $C_2H_3F \rightarrow C_2H_4F$ association rate has not been measured, the above approach cannot be used to deduce a value of E_0 for this reaction. However, *ab initio* and experimental data were used
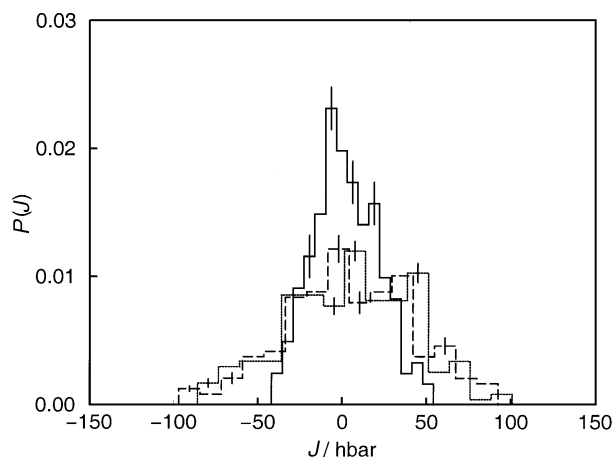

Fig. 3 Distributions of $J_x^{\ddagger}$ (solid line), $J_y^{\ddagger}$ (dashed line) and $J_z^{\ddagger}$ (dotted line) at the $C_2H_3F\cdots H^{\ddagger}$ transition state for the F + $C_2H_4 \rightarrow C_2H_3F + H$ trajectories run on the analytic PES with $E_{rel} = 13.0$ kcal mol^{-1}. $J_z^{\ddagger}$ is the component of J perpendicular to the F–C–C plane and $J_x^{\ddagger}$ is the component lying approximately along the F–C–C axis. Typical error bars are shown by vertical lines.

5 Methods

In much the same way that VENUS96[68] and MOPAC 7.0[69] were interfaced to form the VENUS96–MOPAC package,[70] VENUS96 and GAUSSIAN92[71] were interfaced to perform the *ab initio* direct dynamics simulations reported here. This

allowed the use of all the options in VENUS96 for initializing the trajectories and determining the trajectory results, while obtaining the UHF/6–31G* forces and energy directly from GAUSSIAN92.

5.1 Trajectory initialization

Initial trajectory conditions were chosen so that the simulated results could be compared with the molecular beam data[4,10] obtained for reaction (R1) ($2 \leqslant E_{rel} \leqslant 12$ kcal mol^{-1}), and with the classical trajectory results based on an analytic PES[37] ($E_{rel} = 20$ kcal mol^{-1}). Trajectories were initialized at the exit-channel barrier with total energies, $E^{\ddagger}$, of 14, 19 and 24 kcal mol^{-1} in excess of zero point energy. These energies correspond to $E_{rel} = 8$, 13 and 18 kcal mol^{-1} for the UHF/6–31G* surface [see eqn. (5)].

To investigate the effect of rotation on the E'_{rel} distribution, ensembles of trajectories were initialized at $J = 0$ and $J > 0$. The latter were performed to model the molecular beam experiments for which it is necessary to know at the exit-channel barrier both the distribution of the magnitude of J and its projection on to the principal rotation axes. This information was acquired by propagating complete F + C$_2$H$_4$ → C$_2$H$_3$F + H trajectories on the analytic surface.[37] The coordinates and momenta at the exit-channel barrier (specified by the C$_2$H$_3$F$\cdots$H‡ distance $r_{HC}^{\ddagger} = 1.95$ Å) for these trajectories were used to determine the initial $J > 0$ angular momentum distribution for reactions (R1) and (R2). The C$_2$H$_3$F$\cdots$H‡ coordinates and momenta at the exit-channel barrier were rotated into the principal axis frame by minimizing the sum of squares of the distances of the atomic coordinates from their transition state equilibrium positions in the principle axis frame to find $J_x^{\ddagger}$, $J_y^{\ddagger}$ and $J_z^{\ddagger}$. The distributions for $E_{rel} = 13$ kcal mol^{-1} are shown in Fig. 3 ($J_x^{\ddagger}$ is the component of J that approximately lies along the F–C–C axis and $J_z^{\ddagger}$ the component perpendicular to the F–C–C plane). The calculation of the error bars (vertical lines shown on the histogram), which give the standard deviations, is discussed in Section 5.3. The average values of the magnitudes of the distributions are $\langle J_x^{\ddagger} \rangle = 15.6\hbar$, $\langle J_y^{\ddagger} \rangle = 30.4\hbar$ and $\langle J_z^{\ddagger} \rangle = 31.1\hbar$.

It is interesting to note that the similar values for $\langle J_y^{\ddagger} \rangle$ and $\langle J_z^{\ddagger} \rangle$ and the finding that the probabilities for all three components peak at zero $\hbar$ (consistent with a random projection of J[72]) do not support the kinematic model[10] in which the F atom adds perpendicular to the C$_2$H$_4$, leading to rotation primarily in the FCC plane with $J \approx J_z^{\ddagger} \approx j'$, where j' is the C$_2H_3$F rotational angular momentum. The relative velocity scattering angle distribution $\theta(v,v')$ reported in ref. 37 was not normalized by sin θ and supports the distributions of J components found here and not the model of Farrar and Lee[10] as deduced previously.

The largest J values obtained from the C$_2$H$_4$F classical trajectories (*i.e.*, *ca.* 2% of the ensemble) could not be used to initialize trajectories for reaction (R2) since the sum of the rotational and zero point vibrational energies was larger than the desired trajectory energy. This is because of the smaller principal moments of inertia for C$_2$H$_5^{\ddagger}$ compared with C$_2$H$_4$F‡. As shown below, not including these high values for C$_2$H$_5^{\ddagger}$ has an insignificant effect on the trajectory results.

The system is allocated a certain rotational energy, $E_{rot}^{\ddagger}$, determined from

$$E_{rot}^{\ddagger} = \sum_{i=x,y,z} (J_i^{\ddagger})^2 / 2I_i^{\ddagger} \qquad (6)$$

where the $J_i^{\ddagger}$ are the components of J determined above and the $I_i^{\ddagger}$ are the transition state's principal moments of inertia. The remaining energy is internal energy,

$$E_{int}^{\ddagger} = E^{\ddagger} - E_{rot}^{\ddagger} \qquad (7)$$

and is distributed between the reaction coordinate and vibrational modes. Since the simulation based on the analytic surface showed a statistical distribution of the C$_2$H$_4$F‡ reaction coordinate energy,[37] and since no bottlenecks to intramolecular energy redistribution in the C$_2$H$_4$F complex have been identified, the current work assumes an initial statistical distribution of $E_{int}^{\ddagger}$. As mentioned in the Introduction, this assumption is also consistent with the symmetric C$_2$H$_3$F angular distributions observed experimentally and the dependence of the vibrational product energy on molecular size.[4,10] $E_{int}^{\ddagger}$ was distributed according to a quasi-classical microcanonical sampling of the normal mode vibrational states at the barrier.[49] This yields the quasi-classical analogue of a quantum statistical distributon at the barrier, where all harmonic vibrational levels with energy less than $E_{int}^{\ddagger}$ have equal probability of selection. The difference between $E_{int}^{\ddagger}$ and the energy of the selected vibrational level is placed in the reaction coordinate so as to propel the transition structure towards products. This procedure, which has been detailed elsewhere,[49] leads to a statistical distribution for the reaction coordinate energy and also for the orthogonal vibrational modes. This is illustrated in Fig. 4, where the reaction coordinate energy distribution (histogram) for C$_2$H$_5^{\ddagger}$ at $E^{\ddagger} = 14$ kcal mol^{-1}, $J = 0$, is compared with the RRKM distribution (solid line).[61]

To integrate the trajectories, the components of J, the energies of the vibrational normal modes, and the reaction coordinate energy are transformed to cartesian coordinates and momenta using standard options in VENUS96.[68] This entails choosing a random phase for each normal mode[73] to give normal mode coordinates Q_i and momenta $\dot{Q}_i$ which are then transformed, together with the reaction coordinate, to cartesian coordinates and momenta using the standard linear transformation.[74] Since this is not exact at elevated energies, it is necessary to scale the selected cartesian coordinates and momenta to obtain the desired $E^{\ddagger}$. The scaling factor is $(E^{\ddagger}/E_{scale}^{\ddagger})^{1/2}$, where $E_{scale}^{\ddagger}$ is the total energy of the cartesian coordinates and momenta. The angular momentum may be changed during this scaling, so it is computed and corrected to ensure that $J_x^{\ddagger}$, $J_y^{\ddagger}$ and $J_z^{\ddagger}$ are not altered. Scaling is done iteratively (usually 3–5 steps) until $E_{scale}^{\ddagger}$ is within 0.1% of $E^{\ddagger}$. This scaling is not severe, *e.g.*, for reaction (R1) at $E^{\ddagger} = 19$ kcal mol^{-1} and $J_x^{\ddagger}$, $J_y^{\ddagger}$ and $J_z^{\ddagger}$ chosen as described above, $E_{scale}^{\ddagger}$ and $E^{\ddagger}$ typically agree to within 10–15% before the first scaling.

It should be noted that the total angular momentum for the simulations of the molecular beam experiments may be somewhat overestimated from the trajectories run on the analytic PES. As noted above, the F + C$_2$H$_4$ entrance channel is too
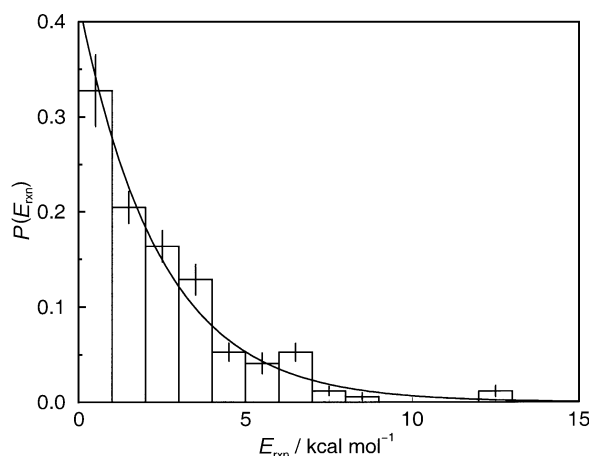

Fig. 4 Normalized reaction coordinate energy distribution at the C$_2$H$_5^{\ddagger}$ transition structure when $E^{\ddagger} = 14$ kcal mol^{-1}, $J = 0$. The RRKM distribution is shown for comparison.

wide for this PES, which may open up reaction for larger impact parameters and, thus, increases the total angular momentum on the reactive system. However, the orbital angular momentum leading to reaction is restricted by the 3 kcal mol^{-1} F + C$_2$H$_4$ → C$_2$H$_4$F barrier on the analytic PES. In addition, classical trajectories do not constrain zero point energy at the exit-channel barrier, which enhances the rate of reaction for large rotational energies. This has the effect of increasing the angular momentum available to the reaction products. A compensating effect, which tends to lower the angular momentum available to the products, is the smaller potential energy difference between the F + C$_2$H$_4$ reactants and the exit-channel barrier for the analytic PES compared with the UHF/6–31G* potential, i.e., 5.5 versus 6.8 kcal mol^{-1}. Regardless of the possible shortcomings, the procedure used here was deemed the best for estimating the C$_2$H$_4$F‡ angular momentum distribution to simulate the molecular beam experiments.

5.2 Trajectory integration

The trajectories were propagated in two ways. In the first, the system's cartesian coordinates and momenta were integrated, while in the second, the instantaneous normal modes determined from the cartesian coordinates[48,75,76] were integrated. The relative merits of these two integration schemes will be discussed in a subsequent paper.[77] Trajectories were integrated until the force between the product fragments was less than 10^{-4} kcal mol^{-1} Å^{-1}, at which time the reaction was considered to be complete. Trajectories were typically propagated for 50–100 fs, and the products were separated by 5.5–6.0 Å. Although the shapes of the energy and angular momentum distributions were apparent after 60–80 trajectories, ensembles of 140–160 trajectories were propagated to improve the statistics.

5.2.1 Cartesian integration.
Newton's equation in cartesian coordinates and momenta was solved using the fixed time step Gauss–Radau integration scheme.[78–80] The cartesian forces and energies were obtained from the converged UHF/6–31G* wavefunction and, by using the optimized molecular orbital coefficients as the initial guess in subsequent force calculations, a significant reduction in computer time was achieved. Trajectories were integrated with a 4.0 fs time step (44 calls to Gaussian per step) which conserved energy to the fifth significant figure. A typical (R2) trajectory was propagated in ca. 176 min on an IBM RS6000/560 computer, which is twice as fast as when using the combined fourth order Runge–Kutta and sixth order Adams–Moulton predictor–corrector algorithm[55,81] standard to VENUS96 (given the same energy conservation).

5.2.2 Normal mode integration.
The normal mode integration scheme[51,82] is based on a local harmonic approximation[83,84] to the PES. Molecular energies, forces and second derivatives, determined using the GAUSSIAN92 series of programs,[71] were used to propagate the system's instantaneous normal modes, which were found by diagonalizing the instantaneous mass-weighted cartesian force constant matrix with the six overall rotational and center of mass translational degrees of freedom projected out.[85] These normal modes are related to the cartesian coordinates by the standard linear transformation.[74]

Recently, a predictor–corrector algorithm which increases the integration efficiency was developed.[51,82] The predictor step, which is based on the local harmonic approximation to the PES, integrates Newton's equation of motion (expressed in terms of the normal modes[83,84] from a point x_i to x_{i+1}^{p} using the energies, forces and second derivatives determined at a

point x_i^p near x_i. The energies, forces and second derivatives determined at x_{i+1}^p are used to fit a polynomial surface to the data at x_i and x_{i+1}^p. The polynomial is fifth order along $x_i - x_{i+1}^p$ and second order in orthogonal directions. The corrector step, based on the polynomial surface, is taken from x_i to x_{i+1}, and allows for a fourfold increase in the integration step size[51] with a similar improvement in the integration efficiency. When the trajectory step size is chosen to conserve energy to the fifth figure, a typical (R2) trajectory is integrated in 81 min when $J = 0$ and 396 min when $J > 0$ (on an IBM RS6000/560 computer).

This normal mode integration is ca. twofold more efficient than the cartesian integration algorithm for $J = 0$. However, with $J > 0$ the cartesian integration method is ca. 2–3-fold more efficient. When the system is rotating, the instantaneous modes found from the projected force constant matrix accurately describe the local motion for only a very short period of time. Strategies, currently under investigation, to improve the normal mode integration with $J > 0$ include only projecting the center of mass translation from the mass-weighted cartesian force constants and adding a rotational velocity component to the instantaneous normal modes with both rotation and translation projected out.

5.3 Analysis of trajectory data

Ensemble averages and distributions were obtained at the exit-channel barrier and for the products. These include the magnitudes of the orbital and rotational angular momenta, $l^\ddagger$, $j^\ddagger$, l' and j', the centrifugal potential $V_{cen}^\ddagger$ and relative translational energy $E_{rel}^\ddagger$ at the barrier, and the product translational, E_{rel}', rotational, E_{rot}', and vibrational, E_{vib}', energies. The centrifugal potential at the barrier is[37]

$$V_{cen}^\ddagger = \frac{(l^\ddagger)^2}{2\mu(r_{rel}^\ddagger)^2} \qquad (8)$$

where $r_{rel}^\ddagger$ is the center of mass displacement between the H atom and the C$_2$H$_3$F/C$_2$H$_4$ fragment at the barrier and μ the corresponding reduced mass.

$E_{rel}^\ddagger$ is

$$E_{rel}^\ddagger = \tfrac{1}{2}\mu\left(\frac{\boldsymbol{v}_{rel}^\ddagger \cdot r_{rel}^\ddagger}{|r_{rel}^\ddagger|}\right)^2 \qquad (9)$$

where $\boldsymbol{v}_{rel}^\ddagger$ is the relative velocity between the H atom and the C$_2$H$_3$F/C$_2$H$_4$ fragment. $E_{rel}^\ddagger$ is similar to (but not identical with) the reaction coordinate energy plotted in Fig. 4. (The dot product between the reaction coordinate eigenvectors shown in Fig. 2 and the unit vector for center of mass separation is 0.91 for C$_2$H$_4$F‡ and 0.92 for C$_2$H$_5$‡.) E_{rel}' of the products was calculated in an equivalent way, i.e.,

$$E_{rel}' = \tfrac{1}{2}\mu\left(\frac{\boldsymbol{v}_{rel}' \cdot r_{rel}'}{|r_{rel}'|}\right)^2 \qquad (10)$$

The total energy at the exit-channel barrier may be expressed as the sum ($E_{rot}^\ddagger + E_{rel}^\ddagger + E_{vib}^\ddagger + V_{cen}^\ddagger + V_{inter}^\ddagger$), where $E_{vib}^\ddagger$ is the vibrational energy of the C$_2$H$_3$F/C$_2$H$_4$‡ fragment and $V_{inter}^\ddagger$ is the C$_2$H$_3$F/C$_2$H$_4$$\cdots$H‡ intermolecular potential. If the fragment's vibrational and rotation energies do not change in moving from the exit-channel barrier to products, and if the exit-channel is isotropic, the product relative translational energy will equal

$$E_{rel}^{iso} = E_{rel}^\ddagger + V_{cen}^\ddagger + E_0 \qquad (11)$$

with $V_{inter}^\ddagger$ equal to E_0. Thus E_{rel}^{iso} was monitored for comparison with E_{rel}'.

Distributions of the trajectory data are presented as normalized histograms, with the data distributed over 16 bins. This number was chosen since it gives ca. 5–20 data points in each bin and produces a histogram that clearly illustrates the

essential features of the distribution. The area under the histogram was normalized to unity.

Since a limited number of data points are used to determine the histograms (140–160 trajectories were propagated in each ensemble), error bars showing the standard deviations were calculated. This was done using the bootstrap method,[86,87] by choosing 100 data points at random from the complete distribution a total of 100 times. The procedure for calculating the standard deviations is the same as in previous applications of the bootstrap method to analyze trajectory results.[88]

5.4 Energetics and normal mode coupling along the IRC

In an investigation similar to that of Kato and Morokuma,[34] the potential energy terms contributing to the exit-channel barrier were identified and intrinsic reaction coordinate (IRC)[85,89] following was performed, in moving from the exit-channel barrier to products, to determine the coupling terms between the reaction coordinate and C_2H_3F/C_2H_4 normal modes of vibration. The classical exit-channel barrier is written as the sum $V_0 = V_{def} + V_{ip}$, where V_{def} is the potential energy due to the deformation of the C_2H_3F/C_2H_4 fragment at the exit-channel barrier from its product equilibrium geometry and V_{ip} is the interaction potential between the dissociating H atom and the C_2H_3F/C_2H_4 fragment. V_{def} was calculated by separating H and C_2H_3F/C_2H_4 by 50 Å so that their interaction energy is zero, while holding the C_2H_3F/C_2H_4 in its transition state geometry. The difference between the resulting potential energy and that for the product, in its equilibrium geometry, is V_{def}. V_{ip} is then $V_0 - V_{def}$. The C_2H_3F/C_2H_4 normal modes that contribute to V_{def} were determined by successively relaxing the out-of-plane modes (dihedrals and wags), in-plane bond angles, and stretches, at a fragment separation of 50 Å, and evaluating the change in energy due to each relaxation.

Couplings between the reaction coordinate and the C_2H_3F/C_2H_4 vibrational modes were determined along the IRC, described in mass-weighted cartesian coordinates. By projecting the change in the reaction coordinate eigenvector along the IRC, dL_r/ds, on to the instantaneous vibrational normal mode eigenvectors, L_{vi}, one obtains the coupling elements

$$C_{rv_i} = \frac{dL_r}{ds} \cdot L_{vi} \qquad (12)$$

where C_{rv_i} is the coupling between the reaction coordinate and mode v_i, and s is the distance from the transition state along the IRC. For each point s, C_{rv_i} gives the change in the reaction coordinate eigenvector (or the gradient of the IRC at s), and determines which of the $3N - 7$ vibrational modes are associated with this change.

In an adiabatic model the quantum states of the vibrational/rotational degrees of freedom do not change in going from the exit-channel barrier to products and, if the vibrational/rotational energy level spacings are similar at the barrier and for the products, all of the exit-channel barrier potential energy goes to product translation. A decrease in the energy level spacings, as for the translational bending modes, can enhance energy transfer to product translation.[29,30] In a sudden[34] model, where the departing H atom is instantaneously separated from the C_2H_3F/C_2H_4 fragment, only the V_{ip} contribution to the exit-channel barrier goes to relative translation. The V_{def} term goes to product vibration.

6 Results and discussion

6.1 Ensemble averages

Table 4 lists ensemble averages obtained at the transition state and for the products for different $E^\ddagger$ and J. $\langle f_{rel} \rangle$, $\langle f_{rot} \rangle$ and $\langle f_{vib} \rangle$ are the fractions of the available energy, E', that are in product relative translation, rotation and vibration, respectively. In the last three rows of the table the angular momentum and its components are chosen to simulate the molecular beam conditions. The entry in the fifth row of the table is for a calculation in which the forces are for the C_2H_5 PES, but with the mass of one of the ethylenic H atoms of the $H\cdots CH_2$ moiety changed to the mass of a F atom to model the kinematics of the $C_2H_3F\cdots H^\ddagger \rightarrow C_2H_3F + H$ reaction.

There is very little change in the average orbital and rotational angular momenta when going from the transition structure to products. Changes in l and j that are found over single trajectories (discussed below) do not affect the ensemble averages. Thus, for the ensemble averaged results, the same angular momentum constraints observed in the previous trajectory study[37] are found in this direct dynamics simulation. The system's total angular momentum J is primarily converted to product (C_2H_4 or C_2H_3F) rotational angular momentum j'. This correlation explains why $\langle f_{rot} \rangle$ significantly increases for the $C_2H_4\cdots H^\ddagger \rightarrow C_2H_4 + H$ simulation when J changes from zero to a distribution representing the molecular beam experiments.

Because of the angular momentum constraints, i.e., $\langle l' \rangle \approx \langle l^\ddagger \rangle$, $\langle V_{cen}^\ddagger \rangle$ is converted to relative product translation. Factors that influence the distribution of the F/H $+ C_2H_4$ reactant relative translational energy between rotational and vibrational energy, and of angular momentum between orbital and rotational angular momentum, will affect $\langle V_{cen}^\ddagger \rangle$ [see eqn. (8)] and hence $\langle E_{rel}' \rangle$. These could include couplings in the entrance channel, which control the impact parameter and orientation of the collision.

There is not a significant change in $\langle f_{rel} \rangle$ when initializing the (R2) trajectories for $J = 0$ or when choosing J to simulate

Table 4 Ensemble averages at the exit channel barrier and for the products[a]

Initial conditions		Transition state				Products					
$E^\ddagger$	J	$E_{rel}^\ddagger$	E_{rel}^{iso}	$l^\ddagger$	$j^\ddagger$	E'	f_{rel}	f_{rot}	f_{vib}	l'	j'
		$C_2H_4\cdots H^\ddagger \rightarrow C_2H_4 + H$									
14.0	0	2.3	6.3	8.8	8.8	17.11	0.38	0.03	0.59	9.1	9.1
19.0	0	2.4	7.6	14.0	14.0	22.11	0.39	0.05	0.56	14.0	14.0
24.0	0	3.0	8.5	14.3	14.3	27.11	0.37	0.05	0.58	14.8	14.8
19.0	Beam[b]	2.5	9.1	17.2	48.4	22.11	0.42	0.38	0.20	18.3	48.1
19.0	Beam[b,c]	2.2	8.4	15.8	51.1	22.11	0.38	0.23	0.39	15.6	51.2
		$C_2H_3F\cdots H^\ddagger \rightarrow C_2H_3F + H$									
19.0	Beam[b]	2.8	12.4	15.7	54.2	25.39	0.50	0.18	0.32	16.8	55.0

[a] Energy is in kcal mol^{-1} and angular momentum in units of $\hbar$. The standard deviation in the average $E_{rel}^\ddagger$, f_{rot} and f_{vib} is ca. 6% and in E_{rel}^{iso}, f_{rel}, $l^\ddagger$, $j^\ddagger$, l' and j' at ca. 3%. [b] The J distribution simulated for $F + C_2H_4 \rightarrow C_2H_3F\cdots H^\ddagger$ is shown in Fig. 5. [c] Forces determined from the C_2H_5 surface, but propagation performed using masses appropriate to the fluorinated reaction (see text).

the beam experiments. There is a decrease in $\langle f_{\text{vib}} \rangle$ for the beam conditions, due to an increase in $\langle f_{\text{rot}} \rangle$. Incorporating the mass of an F atom into the dissociation dynamics (but obtaining the forces from the C_2H_5 PES) does not significantly alter $\langle f_{\text{rel}} \rangle$, but does decrease $\langle f_{\text{rot}} \rangle$ (and thereby increases $\langle f_{\text{vib}} \rangle$) owing to the larger moment of inertia of the fluorinated molecule.

For reaction (R1), $\langle f_{\text{rel}} \rangle = 0.50$, in agreement with experiment. This is larger than $\langle f_{\text{rel}} \rangle$ for reaction (R2), even when the fluorine mass was incorporated into the dynamics. The increase in $\langle f_{\text{rel}} \rangle$ is therefore due to the increase in $E_{\text{rel}}^{\text{iso}}$ for reaction (R1), which is primarily due to the larger exit-channel barrier height.

6.2 Angular momenta and translational energy distributions

Whereas the previous discussion concerned ensemble averaged results, this section focuses on the results obtained for individual trajectories. Data will be presented as normalized histograms, and as correlations between transition state and product properties.

Fig. 5 shows the distributions of orbital and rotational angular momenta for reaction (R2) at $E^{\ddagger} = 19$ kcal mol^{-1}, $J = 0$. The similarity between Fig. 5(a) and (b) arises since $l^{\ddagger} + j^{\ddagger} = l' + j' = J = 0$. There is no broadening or shifting in the l or j distributions on going from the exit-channel barrier to products, indicating that there is no net rotational/orbital angular momentum transfer over the ensemble of trajectories. The orbital and rotational angular momenta are mildly conserved over individual (R2) trajectories when $J = 0$. The $(l^{\ddagger}, l')$ correlation coefficient is 0.75 for reaction (R2) at $E^{\ddagger} = 19$ kcal mol^{-1}, $J = 0$. Owing to the conservation of total angular momentum, the $(j^{\ddagger}, j')$ correlation coefficient is similar to the

$(l^{\ddagger}, l')$ correlation coefficient. Similar angular momentum distributions and correlations are found for reaction (R2) at $E^{\ddagger}$ of 14 and 24 kcal mol^{-1}, $J = 0$.

When initializing trajectories to simulate the molecular beam experiments, the orbital and rotational angular momentum distributions are broader than for $J = 0$. As for $J = 0$, there is no net rotational/orbital angular momentum transfer. The orbital and rotational angular momenta are conserved better than for $J = 0$. For $E^{\ddagger} = 19$ kcal mol^{-1}, the $(l^{\ddagger}, l')$ correlation coefficient for reaction (R2) is 0.87, when incorporating the mass of an F atom into the dynamics it increases to 0.99, and for reaction (R1) it is 0.85.

Fig. 6 shows the E_{rel}' distribution (solid line) for reaction (R2) at $E^{\ddagger} = 19$ kcal mol^{-1}, $J = 0$ (i.e., the same conditions that apply to Fig. 5). Comparison of the E_{rel}' and $E_{\text{rel}}^{\text{iso}}$ (dashed line) distributions shows that there is not a large shift or broadening in the relative translational energy on going from the exit-channel transition structure to products. $P(E_{\text{rel}}')$ is not as symmetric or as broad as that seen experimentally for reaction (R1) (which would have ranged from 0 to $E' \approx 22$ kcal mol^{-1}). In particular, the trajectories do not yield a significant number of large E_{rel}' values ($E_{\text{rel}}' > 16$ kcal mol^{-1}), and the simulated results show a peaking of energies that are lower than the average energy (i.e., the distribution is not symmetric around $\langle E_{\text{rel}}' \rangle = 8.4$ kcal mol^{-1}). Similar results are obtained at $E^{\ddagger}$ of 14 and 24 kcal mol^{-1} for $J = 0$, i.e., there is no shifting or broadening in E_{rel}', and $P(E_{\text{rel}}')$ is narrow.

Fig. 7 shows the product relative translational energy distributions for reaction (R2) at $E^{\ddagger} = 19$ kcal mol^{-1} and when J is chosen to simulate the molecular beam experiment. As for $J = 0$, there is no significant shifting or broadening on going from the exit-channel barrier to products. The distribution in E_{rel}' is broader than for the trajectories propagated with $J = 0$, since $P(E_{\text{rel}}^{\text{iso}})$ is broader, and extends out to the total available energy of ca. 22 kcal mol^{-1}. The broadening in $P(E_{\text{rel}}^{\text{iso}})$ reflects the broadening in $V_{\text{cen}}^{\ddagger}$ under these conditions, as seen when comparing the insets of Fig. 6 and 7. Hence the amount of reactant translational energy that goes to rotational angular momentum and the distribution between rotational and orbital angular momentum at the exit-channel barrier influence the width of the $E_{\text{rel}}^{\text{iso}}$ and E_{rel}' distributions.

Conservations of the relative translational energy on going from the exit-channel barrier to products is mildly retained for individual (R2) trajectories. For $J = 0$, the $(E_{\text{rel}}^{\text{iso}}, E_{\text{rel}}')$ correlation coefficient is 0.77 for $E^{\ddagger} = 14$ kcal mol^{-1}, 0.80 for $E^{\ddagger} = 19$ kcal mol^{-1} and 0.76 for $E^{\ddagger} = 24$ kcal mol^{-1}. Under the molecular beam conditions at $E^{\ddagger} = 19$ kcal mol^{-1} it is
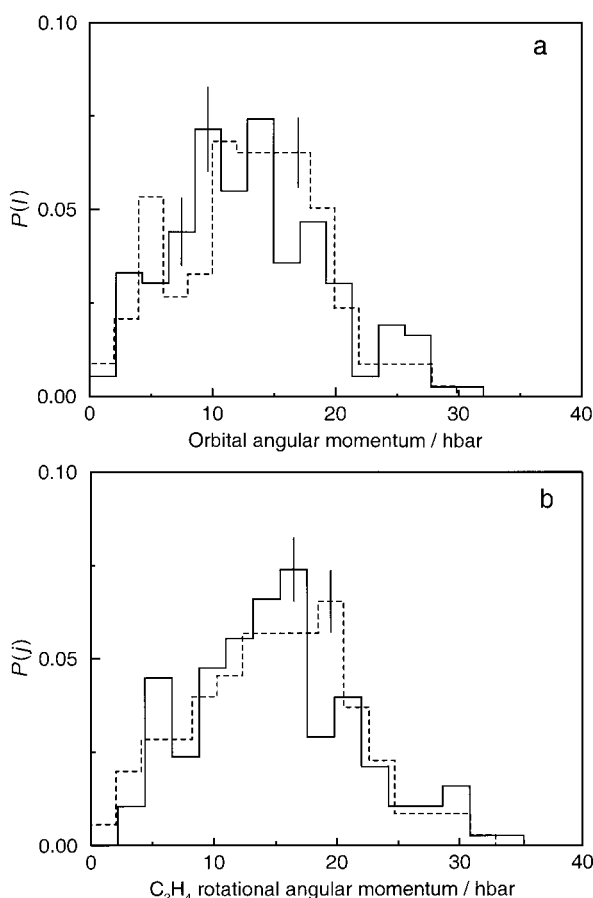
Fig. 5 Normalized distributions of the magnitudes of the (a) orbital and (b) rotational angular momenta for the products (solid line) and at the transition structure (dashed line) for reaction (R2) at 19 kcal mol^{-1} and $J = 0$.
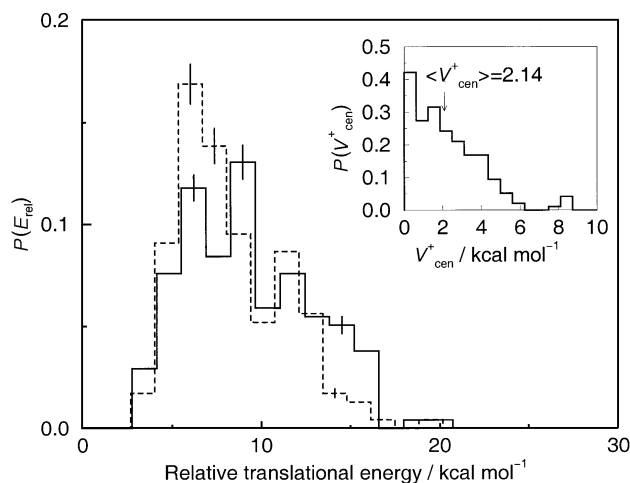
Fig. 6 Normalized distributions of E_{rel}' (solid line) and $E_{\text{rel}}^{\text{iso}}$ (dashed line) for reaction (R2) at 19 kcal mol^{-1}, $J = 0$. The average centrifugal potential at the transition structure is shown together with its normalized distribution in the inset.
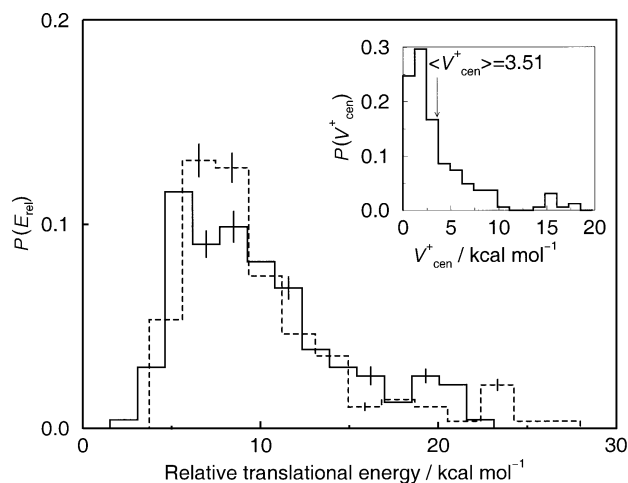
Fig. 7 As Fig. 6 but with the angular momentum chosen to simulate the molecular beam conditions. The initial $J_x^{\ddagger}$, $J_y^{\ddagger}$ and $J_z^{\ddagger}$ distributions are shown in Fig. 3.

Fig. 9 As Fig. 7 but for reaction (R1). The E'_{rel} distribution used to fit molecular beam data for an $F + C_2H_4$ reactant $E_{rel} = 12.1$ kcal mol^{-1} is shown by the dotted curve.

0.84. Since the net gain in translational energy $(E'_{rel} - E^{iso}_{rel} > 0)$ is the same as the net loss $(E'_{rel} - E^{iso}_{rel} < 0)$ over the ensemble, the E^{iso}_{rel} and E'_{rel} distributions are similar.

Substituting the mass of an H atom for that of an F atom in the trajectory dynamics, but obtaining the energies and forces from the C_2H_5 PES, does not significantly alter the E^{iso}_{rel} and E'_{rel} distributions. These are shown in Fig. 8 for $E^{\ddagger} = 19$ kcal mol^{-1} with J chosen to simulate the molecular beam conditions. $P(E'_{rel})$ is similar to $P(E^{iso}_{rel})$ and both distributions are fairly broad owing to the broad distribution of $V_{cen}^{\ddagger}$. The $(E^{iso}_{rel}, E'_{rel})$ correlation coefficient is 0.82, which is similar to that for reaction (R2) under these conditions.

Fig. 9 compares the E'_{rel} and E^{iso}_{rel} distributions for reaction (R1) at $E^{\ddagger} = 19$ kcal mol^{-1} and where J is chosen to simulate the beam conditions. As for reaction (R2), the E^{iso}_{rel} distribution is broadened in the high energy tail owing to a broad $V_{cen}^{\ddagger}$ distribution (see inset). In contrast to reaction (R2), the E'_{rel} distribution is broader than the E^{iso}_{rel} distribution. Coupling in the exit channel leads to a broadening, but not a shifting $(\langle E'_{rel} \rangle \approx \langle E^{iso}_{rel} \rangle)$, of the product translational energy distribution. Since this is not observed for reaction (R2), even when the fluorine mass is incorporated into the dynamics, it is a feature peculiar to dynamics propagated on the C_2H_4F PES. The small $(E^{iso}_{rel}, E'_{rel})$ correlation coefficient of 0.69 shows that relative translational energy is only mildly conserved when going from the exit-channel barrier to products.

The distribution deduced from the molecular beam data[10] for $E_{rel} = 12.1$ kcal mol^{-1} is also shown in Fig. 9 (the simu-
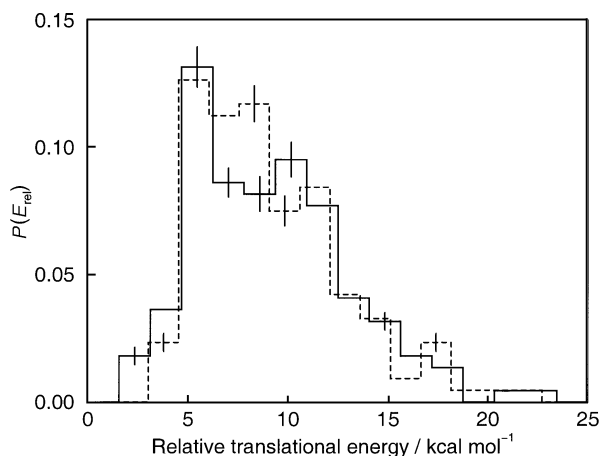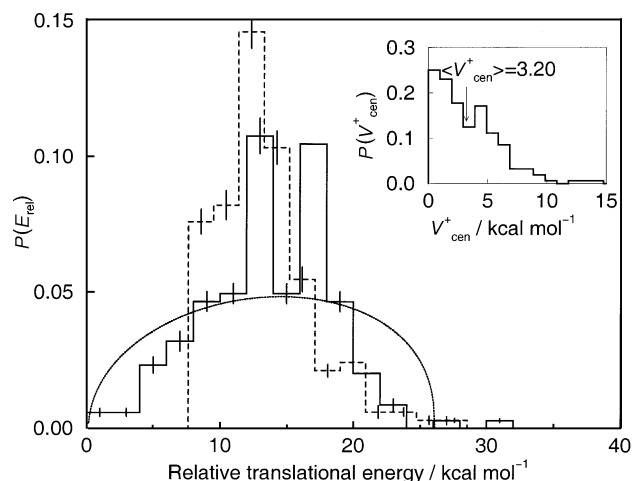
lated $P(E'_{rel})$ is for an E_{rel} of 13 kcal mol^{-1}). The width of the simulated $P(E'_{rel})$ is similar to that of the experimental $P(E'_{rel})$ and ranges from 0 kcal mol^{-1} to the available energy E' of 25.39 kcal mol^{-1}. The differences in the simulated and experimental distributions, e.g., the peaking in the simulated distribution, are probably not important. The experimental distribution is not an observable, but is an assumed functional form that is fit to the experimentally measured data (i.e., the product angular and velocity distributions). The fitting requires a center of mass to laboratory frame transformation which may be insensitive to peaking in $P(E'_{rel})$ as long as the distribution has the proper breadth.

6.3 Energetics and normal mode coupling along the IRC

The direct dynamics trajectories show that, for $E^{\ddagger} = 19$ kcal mol^{-1} with J chosen to simulate the molecular beam conditions, there is a broadening in the E'_{rel} distribution for reaction (R1) but not for (R2). This broadening is not due to $l \leftrightarrow j$ coupling in the exit channel. Apart from l and j being fairly well conserved in the exit-channel dynamics, seen by the fairly large $(l^{\ddagger}, l')$ correlation coefficients of 0.85 and 0.87 for reactions (R1) and (R2), respectively, there is very little correlation between the change in relative product translational energy, $\Delta E = E'_{rel} - E^{iso}_{rel}$, and the change in orbital angular momentum, $\Delta l = l' - l^{\ddagger}$. The $(\Delta E, \Delta l)$ correlation coefficient for reaction (R1) at $E^{\ddagger} = 19$ kcal mol^{-1} with J chosen to simulate the molecular beam experiments is 0.24 and for reaction (R2) it is 0.29. The broadening in $P(E'_{rel})$ seen for reaction (R1) is thus due to coupling between relative translation and the C_2H_3F product vibrations.

The energetic changes that occur as the C_2H_3F/C_2H_4 fragment relaxes on going from transition state to product geometries, and the coupling between the vibrational modes and the reaction coordinate along the IRC gives qualitative information regarding the change in the relative translational energy, E'_{rel}, along the IRC. Although the reaction coordinate eigenvectors at the exit-channel barrier are not associated purely with relative translation (see Fig. 2), the dot product of the reaction coordinate eigenvector with the unit vector describing relative translation—which gives the amount of relative translation character in the reaction coordinate at the transition state—is 0.91 for reaction (R1) and 0.92 for reaction (R2), which shows that the reaction coordinate eigenvector at the exit-channel barrier is primarily relative translation. In the products, the reaction coordinate becomes relative translation

Fig. 8 Fig. 7 but when incorporating the fluorine atomic mass in the dynamics, but using forces relevant to the C_2H_5 PES.

of the product fragments. Couplings between the reaction coordinate and C_2H_3F/C_2H_4 fragment vibrations along the IRC may lead to changes in the reaction coordinate energy.

6.3.1 Deformation and interaction energies.

For reaction (R1), which has an exit-channel barrier (excluding zero point energy) of 6.19 kcal mol^{-1}, V_{def} = 4.39 kcal mol^{-1} and V_{ip} = 1.81 kcal mol^{-1}. Thus, 71% of the barrier is due to deformation of the C_2H_3F fragment. This is slightly lower than the 80% determined by Kato and Morokuma[34] at the UHF/4–31G level of theory. For reaction (R2), which has an exit-channel barrier of 2.91 kcal mol^{-1}, V_{def} = 2.01 kcal mol^{-1} and V_{ip} = 0.90 kcal mol^{-1}; 69% of the barrier is due to deformation of the C_2H_4 fragment. Although the percentages of the barrier due to product deformation are the same for reactions (R1) and (R2), V_{def} for reaction (R1) is more than twice that for reaction (R2). In a sudden model with l and j conserved, E'_{rel} will be less than E^{iso}_{rel} by 4.39 kcal mol^{-1} for reaction (R1) and by 2.01 kcal mol^{-1} for reaction (R2). If the dynamics are intermediate between the sudden and adiabatic models (where $E'_{rel} = E^{iso}_{rel}$), E'_{rel} will differ from E^{iso}_{rel} by between 0 and 4.39 kcal mol^{-1} for reaction (R1) and between 0 and 2.01 kcal mol^{-1} for reaction (R2).

The out-of-plane modes and CC stretch show the largest changes on going from the transition state to product (see Fig. 1 and 2) and are expected to contribute the most to V_{def}. For reaction (R1), 50% of V_{def} is due to out-of-plane deformation and 42% to CC stretch, with most of the remaining 8% being due to CCH and CCF in-plane angle deformations. For reaction (R2), 36% of V_{def} is due to out-of-plane deformation and 63% to CC stretch. In the sudden model for reaction (R1), the normal modes that have large out-of-plane character (v_5, v_6, v_8 and to a lesser extent v_4 and v_7) and CC stretch (v_{12}) will gain most of V_{def}, with the combined energy in the out-of-plane modes being more than the energy in the CC stretch mode. In the sudden model for reaction (R2), the out-of-plane modes (v_5, v_6 and v_7) will gain 36% of V_{def} and the CC stretch mode (v_8) will gain 63%. If the exit-channel dynamics of reactions (R1) and (R2) have features of both the adiabatic and sudden models, and if the out-of-plane and CC stretch normal modes are coupled to the reaction coordinate, then these modes may exchange energy with the reaction coordinate, some of which will be V_{def}.

6.3.2 Reaction coordinate coupling along the IRC.

The coupling between the reaction coordinate and the fragment vibrational modes, as defined in eqn. (12), are shown in Fig. 10 and 11 for reactions (R1) and (R2), respectively. Only the vibrational modes showing the largest coupling are shown; the reaction coordinate coupling with the other modes never exceeds 0.07 at any point along the IRC. The modes that couple strongest to the reaction coordinate are the out-of-plane and CC stretch modes, i.e., the same modes that gain V_{def} in the sudden model. This is not surprising since it is these modes that deviate the most between the transition state and product geometries, and their change on going from transition state to product will be reflected in the reaction coordinate eigenvector at some stage along the IRC.

More modes are coupled to the reaction coordinate for reaction (R1) than for reaction (R2), and the coupling is, in general, stronger for reaction (R1). Energy flow between the reaction coordinate and fragment vibrational modes may therefore be more rapid and more extensive for reaction (R1), leading to the larger differences in E'_{rel} and E^{iso}_{rel} for reaction (R1). This was observed in the direct dynamics simulation. For both reactions (R1) and (R2), the out-of-plane vibrational modes couple strongest to the reaction coordinate. In the sudden model these modes have 50% of V_{def} (2.2 kcal mol^{-1})
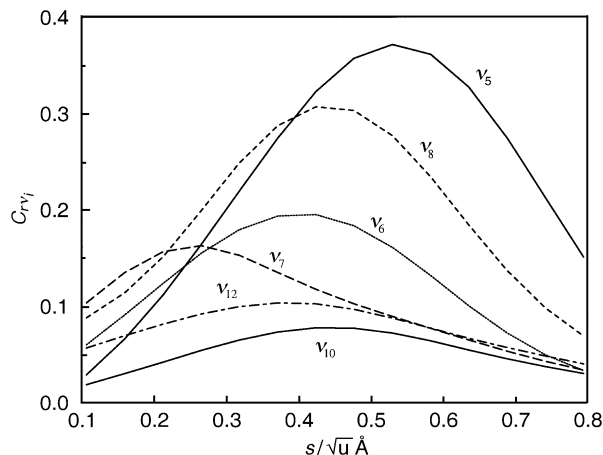

Fig. 10 Coupling between the reaction coordinate and C_2H_3F vibrational modes along the IRC for reaction (R1). Only the vibrational modes with the largest coupling are shown. v_5, v_6, v_7 and v_8 are out-of-plane modes, v_{10} is in-plane CHF bend and v_{12} is CC stretch.

for reaction (R1) and 36% (0.73 kcal mol^{-1}) for reaction (R2). Hence a larger part of V_{def} may flow to the reaction coordinate for reaction (R1) than for reaction (R2).

7 Conclusions

The direct dynamics technique, using energies, forces and second derivatives obtained at the UHF/6–31G* level of theory, has been used to propagate $C_2H_4F^{\ddagger} \rightarrow C_2H_3F + H$ and $C_2H_5^{\ddagger} \rightarrow C_2H_4 + H$ trajectories from the exit-channel barrier to products, facilitating investigations of exit-channel coupling effects on the product energy distributions. This work illustrates the feasibility of using the direct dynamics method to study chemical systems, even at relatively high levels of electronic structure theory.

The ensemble averaged properties for both reactions are well described by a model that incorporates angular momentum constraints when going from the barrier to products. This is valid at all energies and angular momenta investigated. Since the orbital angular momentum is conserved, the centrifugal potential at the exit-channel barrier, $V_{cen}^{\ddagger}$, is converted to E'_{rel}. Also, since vibrational coupling in the exit channel does not lead to extensive shifts in the relative translational energy, a model based on isotropic exit-channel dynamics
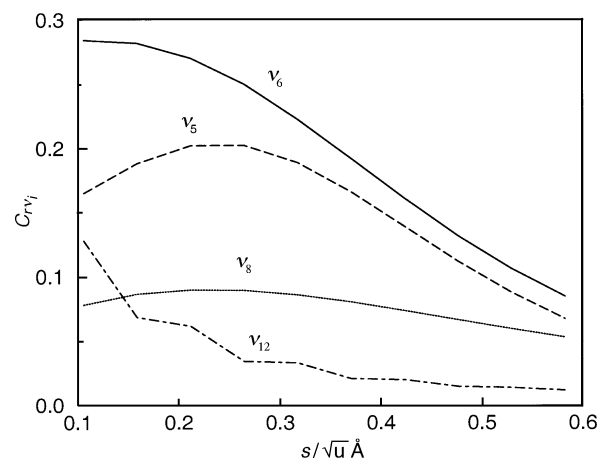

Fig. 11 Fig. 10 but for reaction (R2). v_5 and v_6 are out-of-plane modes and v_8 and v_{12} are CC stretches.

gives very good agreement with the ensemble averaged trajectory results.

The isotropic model is not valid for individual trajectories. For reaction (R2) there is no net effect of coupling in the exit channel, and the distribution of E'_{rel} is the same as that of E^{iso}_{rel}. The broadening in the E^{iso}_{rel} distribution observed when the angular momentum is chosen to simulate the molecular beam experiments, is reflected in a similar broadening in the E'_{rel} distribution. For reaction (R1), the E'_{rel} distribution is broader than the E^{iso}_{rel} distribution, although the distributions have similar average values.

If a statistical population of vibrational energy levels at the exit-channel transition state is assumed, and the angular momentum is chosen to represent the molecular beam experiment, the UHF/6–31G* direct dynamics E'_{rel} distribution is similar to the distribution deduced from crossed molecular beam experiments, and the average fraction of the available energy that goes to product translation is the same, i.e., 0.5.

The difference in the exit-channel dynamics for reactions (R1) and (R2) is due to differences in the exit-channel energetics and/or coupling between the relative translation and C_2H_3F/C_2H_4 fragment vibrations. In a sudden model, twice as much energy goes to product vibration for reaction (R1) than reaction (R2). The vibrational modes that gain this energy, i.e., the out-of-plane and CC stretch modes, are coupled to the reaction coordinate along the IRC. More modes are coupled to the reaction coordinate for reaction (R1) than (R2), and the coupling is, in general, stronger. Thus, the flow of energy between the reaction coordinate and the product vibrational modes may be faster and more extensive for reaction (R1) than reaction (R2). This explains the larger differences between E'_{rel} and E^{iso}_{rel} for reaction (R1), leading to a broadening in the E'_{rel} distribution observed in the direct dynamics simulation and molecular beam experiments.

An RRKM analysis showed that a secondary reaction pathway, involving 1–2 hydrogen migration before C_2H_4F decomposition, is not significant for forming the $C_2H_3F + H$ products. The majority of products observed in the molecular beam experiment are formed from H dissociating from the carbon to which the fluorine is attached. This is the reaction pathway studied in the direct dynamics simulation.

Acknowledgements

References

1 D. R. Lide, Jr. and D. Christensen, *Spectrochim. Acta*, 1961, **17**, 665.
2 M. C. Lin and M. H. Back, *Can. J. Chem.*, 1966, **44**, 2357.
3 L. F. Loucks and K. J. Laidler, *Can. J. Chem.*, 1967, **45**, 2795.
4 J. M. Parson and Y. T. Lee, *J. Chem. Phys.*, 1972, **56**, 4658.
5 J. L. Duncan, I. J. Wright and D. Van Lerberghe, *J. Mol. Spectrosc.*, 1972, **42**, 463.
6 W. E. Jones, S. D. MacKnight and L. Teng, *Chem. Rev.*, 1973, **73**, 407.
7 J. V. Michael and G. N. Suess, *Chem. Phys.*, 1973, **58**, 2807.
8 J. G. Moehlmann, J. T. Gleaves, J. W. Hudgens and J. D. McDonald, *J. Chem. Phys.*, 1974, **60**, 4790.
9 J. A. Cowfer and J. V. Michael, *Chem. Phys.*, 1975, **62**, 3504.
10 J. M. Farrar and Y. T. Lee, *J. Chem. Phys.*, 1976, **65**, 1414.
11 J. H. Lee, J. V. Michael, W. A. Payne and L. J. Stief, *J. Chem. Phys.*, 1978, **68**, 1817.
12 M. G. Moss, M. D. Ensminger, G. M. Stewart, D. Mordaunt, and J. D. McDonald, *J. Chem. Phys.*, 1980, **73**, 1256.
13 G. V. Pukals'kaya, N. F. Chebotarev, V. B. Kolovskii and S. Ya. Pashezhetskii, *Kinet. Katal.*, 1980, **21**, 1063.
14 K. Sugawara, K. Okuzaki and S. Sato, *Chem. Phys. Lett.*, 1981, **78**, 259, *Bull. Chem. Soc. Jpn.*, 1981, **54**, 2872.
15 P. D. Pacey and J. H. Wimalasena, *J. Phys. Chem.*, 1984, **88**, 5657.
16 A. B. Trenwith, *J. Chem. Soc., Faraday Trans. 2*, 1986, **82**, 457.
17 P. D. Lightfoot and M. J. Pilling, *J. Phys Chem.*, 1987, **91**, 3373.
18 Y. Simon, J. F. Foucaut and G. Scacchi, *Can. J. Chem.*, 1988, **66**, 2142.
19 J. W. Davies and M. J. Pilling. In *Bimolecular Reactions*, ed. M. N. R. Ashfold and J. E. Baggott, Royal Society of Chemistry, London, 1989, pp. 171–208.
20 G. N. Robinson, R. E. Continett and Y. T. Lee, *J. Chem. Phys.*, 1990, **92**, 275.
21 M. A. Hanning-Lee, N. J. B. Green, M. J. Pilling and S. H. Robertson, *J. Phys. Chem.*, 1993, **97**, 860.
22 Y. Feng, J. T. Niiranen, A. Benosura, V. D. Knyazev, D. Gutman and W. Tsang, *J. Phys. Chem.*, 1993, **97**, 871.
23 R. A. Marcus, *J. Chem. Phys.*, 1975, **62**, 1372.
24 G. Worry and R. A. Marcus, *J. Chem. Phys.*, 1977, **67**, 1636.
25 V. B., Kontecky, K. Kontecky and L. Salem, *J. Am. Chem. Soc.*, 1977, **99**, 842.
26 D. J. Zvijac and L. C. Light, *Chem. Phys.*, 1977, **21**, 411; D. J. Zvijac, S. Mukamel and J. Ross, *Chem. Phys.*, 1977, **67**, 2007.
27 C. S. Sloane and W. L. Hase, *Faraday Discuss. Chem. Soc.*, 1977, **62**, 210.
28 W. L. Hase, G. Mrowka, R. J. Brudzynski and C. S. Sloane, *Faraday Discuss. Chem. Soc.*, 1978, **69**, 3548; 1980, **72**, 6321.
29 D. T. Clar, I. W. Scanlan and J. C. Walton, *Chem. Phys. Lett.*, 1978, **55**, 102.
30 W. L. Hase, R. J. Wolf and C. S. Sloane, *J. Chem. Phys.*, 1979, **71**, 2911, 1982, **76**, 2771.
31 S. Nagase, T. Fueno and K. Morokuma, *J. Am. Chem. Soc.*, 1979, **101**, 5849.
32 M. Quack, *Chem. Phys.*, 1980, **51**, 353.
33 S. Nagase and C. W. Kern, *J. Am. Chem. Soc.*, 1980, **102**, 4513.
34 S. Kato and K. Morokuma, *J. Chem. Phys.*, 1980, **72**, 206.
35 L. B. Hardin, *J. Am. Chem. Soc.*, 1981, **103**, 7469.
36 W. L. Hase, D. M. Ludlow, R. J. Wolf and T. J. Schlick, *J. Phys. Chem.*, 1981, **85**, 958.
37 W. L. Hase and K. C. Bhalla, *J. Chem. Phys.*, 1981, **75**, 2807.
38 W. L. Hase and D. G. Buckowski, *J. Comput. Chem.*, 1982, **3**, 335.
39 W. L. Hase and H. B. Schlegel, *J. Phys. Chem.*, 1982, **86**, 3901.
40 H. B. Schlegel, *J. Phys. Chem.*, 1982, **86**, 4878.
41 H. B. Schlegel, K. C. Bhalla and W. L. Hase, *J. Phys. Chem.*, 1982, **86**, 4883.
42 W. L. Hase, D. G. Buckowski and K. N. Swamy, *J. Phys. Chem.*, 1983, **87**, 2754.
43 K. N. Swamy and W. L. Hase, *J. Phys. Chem.*, 1983, **87**, 4715.
44 J. C. Light, *J. Chem. Phys.*, 1964, **40**, 3221.
45 P. Pechukas and J. C. Light, *J. Chem. Phys.*, 1965, **42**, 3281.
46 S. A. Safron, N. D. Weinstein, D. R. Herschbach and J. C. Tully, *Chem. Phys. Lett.*, 1972, **12**, 564.
47 G. H. Peslherbe, H. Wang and W. L. Hase, *J. Am. Chem. Soc.*, 1996, **118**, 2257.
48 G. H. Peslherbe and W. L. Hase, *J. Chem. Phys.*, 1996, **104**, 7882.
49 C. Doubleday, Jr., K. Bolton, G. H. Peslherbe and W. L. Hase, *J. Am. Chem. Soc.*, 1996, **118**, 9922; K. Bolton, W. L. Hase and C. Doubleday, Jr, *Ber. Bunsen-Ges. Phys. Chem.*, 1997, **3**, 414.
50 C. Doubleday, Jr, K. Bolton and W. L. Hase, *J. Am. Chem. Soc.*, 1997, **119**, 5251; C. Doubleday, Jr, K. Bolton and W. L. Hase, *J. Phys. Chem. A*, 1998, **102**, 3648.
51 W. Chen, W. L. Hase and H. B. Schlegel, *Chem. Phys. Lett.*, 1994, **228**, 436.
52 K. Bolton, W. L. Hase and G. H. Peslherbe, in *Modern Methods for Multidimensional Computations in Chemistry*, ed. D. L. Thompson, Wold Scientific, Singapore, 1998, p. 143.
53 J. Ishctwan and M. A. Collins, *J. Chem. Phys.*, 1994, **100**, 8080; M. J. T. Jordan, K. C. Thompson and M. A. Collins, *J. Chem. Phys.*, 1995, **102**, 5647.
54 T.-S. Ho and H. Rabitz, *J. Chem. Phys.*, 1996, **104**, 2584; T.-S. Ho, T. Hollebeek, H. Rabitz, L. B. Harding and G. C. Schatz, *J. Chem. Phys.*, 1996, **105**, 10472.
55 D. G. Truhlar and J. T. Muckerman. In *Atom–Molecule Collision Theory*, ed. R. B. Bernstein, Plenum Press, New York, 1979, pp. 505–566.
56 G. C. *J. Chem. Phys.*, 1983, **79**, 5386.
57 K. Bolton, W. L. Hase, H. B. Schlegel and K. Song, *Chem. Phys. Lett.*, 1998, **288**, 621.
58 A. P. Scott and L. Radom, *J. Phys. Chem.*, 1996, **100**, 16502.
59 Since the barriers for $C_1 \cdots H$ bond rupture and $C_1 \to C_2$ migration are sharp (the QCISD/6–311G** $C_1 \cdots H$ and $C_1 \to C_2$ reac-

tion coordinate harmonic frequencies are 1043i cm^{-1} and 2199i cm^{-1}, respectively), it is assumed that the transition state structures are similar to those at the potential barriers. For the future, more detailed calculations it would be of interest to consider variational effects in choosing the transition state; J. Villa, A. Gonzalez-Lafont, J. M. Lluch and D. G. Truhlar, *J. Am. Chem. Soc.*, 1998, **120**, 5559.

60 R. G. Gilbert and S. C. Smith, *Theory of Unimolecular and Recombination Reactions*, Blackwell, Oxford, 1990.
61 T. Baer and W. L. Hase, *Unimolecular Reaction Dynamics: Theory and Experiments*, Oxford University Press, New York, 1996.
62 L. Zhu, W. Chen, W. L. Hase and E. W. Kaiser., *J. Phys. Chem.*, 1993, **97**, 311.
63 *CRC Handbook of Chemistry and Physics*, ed. D. R. Lide, CRC Press, Boca Raton, 78th edn., 1997.
64 J. L. Duncan, D. C. McKean and P. D. Mallinson, *J. Mol. Spectrosc.*, 1973, **45**, 221.
65 G. R. Smith and W. A. Guillory, *J. Phys. Chem.*, 1975, **63**, 1311.
66 D. A. McQuarrie, *Statistical Mechanics*, Harper Collin, New York, 1976.
67 W. L. Hase, H. B. Schlegel, V. Balbyshev and M. Page, *J. Phys. Chem.*, 1996, **100**, 5354; W. L. Hase, H. B. Schlegel, V. Balbyshev and M. Page, *J. Phys. Chem. A*, 1997, **101**, 5026.
68 W. L. Hase, R. J. Duchovic, X. Hu, A. Kormonick, K. Lim, D.-H. Lu, G. H. Peslherbe, K. N. Swamy, S. R. Vande Linde, A. J. C. Varandas, H. Wang and R. J. Wolfe, *QCPE*, 1996, **16**, 671. VENUS96 is an enhanced version of MERCURY; W. L. Hase, *QCPE*, 1983, **3**, 453.
69 J. P. P. Stewart, *QCPE*, 1993, **13**, 455; *J. Comput. Chem.*, 1989, **10**, 209.
70 G. H. Peslherbe, W. L. Hase, *VENUS–MOPAC, a General Chemical Dynamics and Semiempirical Direct Dynamics Computer Program*, to be released.
71 M. J. Frisch, G. W. Trucks, M. Head-Gordon, P. M. W. Gill, J. B. Foresman, M. W. Wong, B. G. Johnson, H. B. Schlegel, M. A. Robb, E. S. Replogle, R. Gomperts, J. L. Andres, K. Raghavachari, J. S. Binkley, C. Gonzalez, R. L. Martin, D. J. Fox, D. J. DeFrees, J. Baker, J. J. P. Stewart and J. A. Pople. *GAUSSIAN92*, Gaussian, Pittsburgh, PA, 1992.
72 D. L. Bunker and W. L. J. Hase, *Chem. Phys.*, 1973, **59**, 4621.
73 S. Chapman and D. L. Bunker, *J. Chem. Phys.*, 1975, **62**, 2890; C. S. Sloane and W. L. Hase, *Chem. Phys.* 1977, **66**, 1523.
74 E. B. Wilson, Jr, J. C. Decius and P. C. Cross, *Molecular Vibrations*, McGraw-Hill, New York, 1955.
75 W. H. Miller, W. L. Hase and C. L. Darling, *J. Chem. Phys.*, 1989, **91**, 2863.
76 J. E. Adams and R. M. Stratt, *J. Chem. Phys.*, 1990, **93**, 1332.
77 K. Bolton, W. L. Hase and H. B. Schlegel, to be submitted.
78 E. Everhart, *Celest. Mech.*, 1974, **10**, 35.
79 E. Everhart, in *Dynamics of Comets: Their Origin and Evolution*, ed. A. Carusi and G. B. Valsecchi, Reidel, Dordrecht, 1985, pp. 185–202.
80 K. Boltan and S. Nordholm, *J. Comput. Phys.*, 1994, **113**, 320.
81 W. H. Press, S. A. Teukolsky, W. T. Vetterling and B. P. Flannery, *Numerical Recipes in Fortran; the Art of Scientific Computing*, Cambridge University Press, Cambridge, 1992.
82 W. Chen, PhD Thesis, Wayne State University, 1995.
83 T. Helgaker, E. Uggerud and H. Jensen, *Chem. Phys. Lett.*, 1990, **173**, 145.
84 E. Uggerud and T. Helgaker, *J. Am. Chem. Soc.*, 1992, **114**, 4266.
85 W. H. Miller, N. C. Handy and J. E. Adams, *J. Chem. Phys.*, 1980, **72**, 99.
86 B. Efron, *SIAM Rev.*, 1979, **21**, 460.
87 P. Diaconis and B. Efron, *Sci. Am.*, 1983, **248**, 96.
88 H. W. Schranz, S. Nordholm and B. C. Freasier, *Chem. Phys.*, 1986, **108**, 69; D. L. Clarke, I. Oref, R. G. Gilbert and K. F. Lim, *J. Chem. Phys.*, 1992, **96**, 5983; K. Bolton, S. Nordholm and H. W. Schranz, H. W. *J. Phys. Chem.*, 1995, **99**, 2477.
89 D. G. Truhlar and A. Kupperman, *J. Am. Chem. Soc.*, 1971, **93**, 1840.
90 M. Quack and J. Troe, *Ber. Bunsen-Ges. Phys. Chem.*, 1974, **78**, 240; 1975, **79**, 170; 1976, **80**, 1140.

Paper 8/08650H